COMMUNICATION

Microporous carbon nanosheets with redox-active heteroatoms for pseudocapacitive charge storage†

Y. S. Yun,[a] D.-H. Kim,[a] S. J. Hong,[b] M. H. Park,[c] Y. W. Park,[b] B. H. Kim,[d] H.-J. Jin*[c] and K. Kang*[a,e]

We report microporous carbon nanosheets containing numerous redox active heteroatoms fabricated from exfoliated waste coffee grounds by simple heating with KOH for pseudocapacitive charge storage. We found that various heteroatom combinations in carbonaceous materials can be a redox host for lithium ion storage. The bio-inspired nanomaterials had unique characteristics, showing superior electrochemical performances as cathode for asymmetric pseudocapacitors.

Nanostructured carbonaceous materials (NCMs) have recently received attention as faradic electrodes for energy storage.[1–9] Nanometer-size effects such as nanoionics[10] and nanoelectronics[11] enable fast ion/electron transfer, resulting in high rate performance.[12] In addition, the large surface-to-volume ratio accelerates surface-driven reactions, leading to high charge storage and highly stable cycles. In particular, the possibility of developing advanced power sources, which exhibit high power, large energy output and stable cyclic performance, has been realised by using NCMs as both anode and cathode as faradic electrode pairs.[1,13–15]

For cathodes, several groups have recently reported NCMs containing oxygen redox centres in which lithium ions can be stored pseudocapacitively.[1,2,4,14] Kim *et al.* reported that energy and power can be tuned by controlling the degree of oxygen functional groups on graphene-based nanosheets (GNSs), indicating that energy and power are in conflict with each other.[2] More oxygen redox centres led to an increase in energy density but a decrease in power density, due to an unfavourable electrical property induced by more oxidised

sites. One possible strategy to boost both energy and power in oxygen-functionalised NCMs is doping of additional heteroatoms in the carbon structure, which can increase the electrical properties of the NCMs by N-type doping effects[8,16] and also function as a redox centre for greater charge storage.[17,18] Nevertheless, there have been few studies utilising additional nitrogen and/or sulphur doping on NCMs with the objective of improving their electrochemical performance as cathodes. Meanwhile, Ding *et al.* reported that highly porous nanocarbons containing oxygen redox centres showed excellent rate capabilities with stable cyclic performances as cathodes for lithium-ion storage.[19] This result clarified that (1) the kinetics of the surface-driven charge storage are dependent on the active surface area, and (2) a porous carbon structure can mitigate fatigue originating from repetitive cycles. Thus, the synergistic effects of additional redox-active heteroatoms, high electrical conductivity and a porous carbon structure with high surface area may maximise the electrochemical performance of NCM-based cathodes.

Coffee is one of the most abundant agricultural commodities, with a global production of approximately eight million metric tons per year; most of this is discarded as waste coffee grounds (WCGs) by beverage manufacturers.[20] WCGs are mainly composed of lignocellulose containing aromatic polymers,[21] and considered to be good carbon precursors;[21–25] with lignocellulose exhibiting a high carbon yield at a fast heating rate of 20 °C min^{-1}.[26] In addition, WCGs have diverse components with numerous heteroatoms (*e.g.* nitrogen, oxygen, and sulphur), which can be possibly doped on the carbon structure by heating. Studies to fabricate porous carbon materials from WCGs have shown that they exhibit good electrochemical performance as an electrode for electrostatic charge storage.[23–25] However, a nanostructured design for pseudocapacitive charge storage has not been investigated.

In this study, functionalised and microporous carbon nanosheets (FM-CNSs) were fabricated from exfoliated WCGs by simple heat treatment with KOH. The WCG-inspired carbon materials facilitate 4.3 at% nitrogen and 2.1 at% sulphur as well as 20.5 at% oxygen functional groups with no additional

[a]Department of Materials Science and Engineering, Seoul National University, Seoul 151-742, South Korea. E-mail: matlgen1@snu.ac.kr

[b]Department of Physics and Astronomy, Seoul National University, Seoul 151-747, South Korea

[c]Department of Polymer Science and Engineering, Inha University, Incheon 402-751, South Korea. E-mail: hjjin@inha.ac.kr

[d]Department of Physics, Incheon National University, Incheon 406-772, South Korea

[e]Center for Nanoparticle Research, Institute for Basic Science (IBS), South Korea

†Electronic supplementary information (ESI) available. See DOI: 10.1039/c5nr04231c

doping process. Moreover, a 2D-like nanostructure with a high surface area of ~2100 m² g⁻¹ was developed in the heating process. These unique material properties can lead to good electrochemical performance, which exceed those of well-defined and -tailored carbon materials such as graphene-based nanosheets (GNSs). Our results demonstrate that asymmetric hybrid pseudocapacitors based on FM-CNSs have outstanding energy and power characteristics that excel all the previously reported carbon-based pseudocapacitors, indicating a potential for EV applications.

Results and discussion

The FM-CNSs have irregular shapes and different sizes, however, their morphologies are close to 2D-like nanosheets with a lateral size of several micrometres and a thickness of ~9 nm [Fig. 1(a) and (d)]. Field emission transmission electron microscopy (FE-TEM) images also show the ultra-thin nanosheet shape with an amorphous carbon structure [Fig. 1 (b) and (c)]. These unique 2D morphologies are apparently distinct from WCG-induced carbon after heating without exfoliation and KOH activation [Fig. S1†]. In the first exfoliation process, in organic solvent dimethylformamide (DMF), WCG particles splinter. Following *in situ* carbonisation and activation using KOH, the WCG particles split further and transform the aliphatic carbon structure into an aromatic carbon structure containing numerous heteroatoms and micropores [Fig. S1†]. The XRD patterns of FM-CNSs exhibit broad graphi-

tic (002) and (100) peaks, indicating poor development of the graphitic crystal structure [Fig. 1(e)]. In contrast, Raman spectroscopy clearly shows the main D and G band peaks. The D band corresponds to the disorder in the A_{1g} breathing mode of the six-fold aromatic ring near the basal edge, and the G band reflects the hexagon structure related to the E_{2g} vibration mode of the sp²-hybridised C atoms [Fig. 1(f)]. The I_D/I_G intensity ratio is about ~0.92, indicating that the ordered hexagonal structure is several nanometres in size; thus, the amorphous carbon structure of FM-CNSs comprises numerous nanometre-sized crystallites with random orientation.[27] The structure is also identified in the temperature-dependent electrical transport properties of FM-CNSs (Fig. 1(g)). The current–voltage (*I–V*) characteristics are highly symmetric and linear in the low bias regime (<10 mV) throughout temperature regions from 20 K to 300 K. At room temperature, the conductivity of FM-CNSs was found to be 120 S cm⁻¹, which is unusually high for an amorphous carbon structure and is 400-fold higher than the 0.3 S cm⁻¹ found in GNSs fabricated by chemical methods.[8] It is likely that the remaining electrons of the doped heteroatoms donate free carriers, contributing to the overall conductivity of FM-CNSs. The temperature-dependent conductivity ($\sigma(T)$) increases with temperature, as shown in blue scatters in Fig. 1(h), indicating that FM-CNSs follow non-metallic behaviour. Analysing the $\sigma(T)$, we found that fluctuation induced tunnelling (FIT) was the charge transport mechanism of the FM-CNS system. FIT is often observed in inhomogeneous materials, which consist of a large conducting region and small insulating barrier.[28] The microstructure of FM-CNSs based on XRD and Raman spectroscopy (schematically shown in Fig. S2†) is in a good agreement with the FIT model. $\sigma(T)$ is well fitted by $\sigma(T) = \sigma_0 \exp\left(-\dfrac{T_1}{T + T_0}\right)$ (red dotted line of Fig. 1(h)), where T_1 is the temperature corresponding the energy scale for electrons to overcome the barrier and T_0 is the temperature below which tunnelling dominates.[29] T_1 and T_0 are given by $T_1 = \dfrac{8\varepsilon_0 A V_0^2}{e^2 k_B w}$, $T_0 = \dfrac{16\varepsilon_0 \hbar A V_0^{3/2}}{\pi e^2 k_B (2m)^{1/2} w^2}$, where w is the width of the tunnelling gap, A is the area of the capacitance formed by the tunnel junction, V_0 is the height of the potential barrier, k_B is the Boltzmann constant, e is the electric charge, m is the effective electron mass, and ε_0 is the vacuum permittivity. Note that the fitting parameters are T_1 = 89.4 K, T_0 = 104 K, and σ_0 = 147 S cm⁻¹, respectively. Porous properties are characterised by nitrogen adsorption and desorption experiments. The nitrogen adsorption and desorption isotherm curves shown in Fig. 1(i) are indicative of an IUPAC type-I microporous structure. The Brunauer–Emmett–Teller (BET)-specific surface area of the FM-CNSs was 2100 m² g⁻¹, and the width of most micropores was less than a nanometre [see the inset of Fig. 1(i)]. In particular, ultramicropores (<0.7 nm) are dominant,[29] and the micropore volume (0.947 cm³ g⁻¹) ratio *versus* single point adsorption total pore volumes (1.003 cm³ g⁻¹) was about 0.95, indicating the distinct pore structure of FM-CNSs compared with conventional porous carbons.[30]
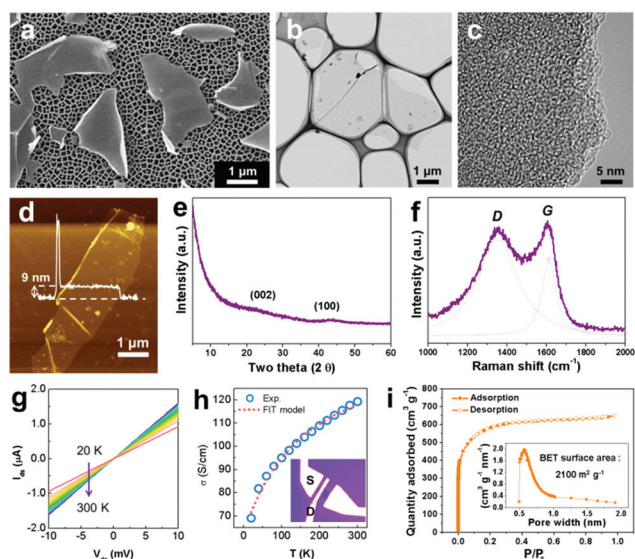

Fig. 1 Characteristics of FM-CNSs. (a) FE-SEM image of samples deposited on a porous alumina template and (b), (c) FE-TEM images with different magnifications. (d) AFM topographic image of a sample. (e) XRD data and (f) Raman spectrum of samples. (g) Temperature-dependent electrical transport properties measured from 20 K to 300 K with a step of 20 K. (h) Temperature-dependent conductivity curves obtained from *I–V* curves and FIT model, and inset of optical image of the two-electrode configuration. (i) Nitrogen adsorption and desorption isotherm curves and inset is pore size distribution.
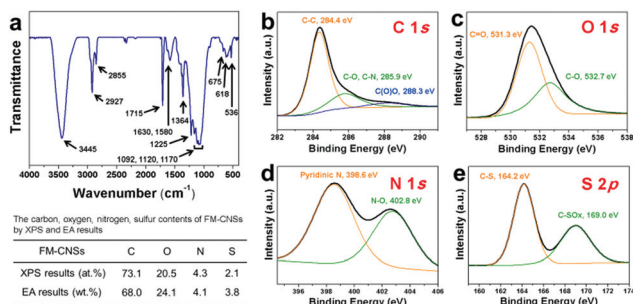
Fig. 2 Chemical configurations of FM-CNSs. (a) FT-IR spectrum, and XPS (b) C 1s, (c) O 1s, (d) N 1s and (e) S 2p spectra.

Surface properties of the FM-CNSs are investigated by Fourier transform infrared (FT-IR) spectroscopy [Fig. 2(a)]. The FT-IR spectrum of the FM-CNSs shows the presence of various oxygen functional groups such as O–H, C=O, C–O, C–O–C and epoxide at 3445, 1715, 1092, 1120 and 1170 cm^{-1}. A peak of aromatic nitrogen compounds and a stretching vibration peak of pyridine N-oxide at 1364 and 1225 cm^{-1}, respectively, are observed with a N–O_2 rocking vibration peak at 618 cm^{-1}. In addition, the FT-IR spectrum shows the characteristic sulphur bonding such as a C–S stretching vibration peak and C–S=O in-plane deformation vibration peak at 675 and 536 cm^{-1}, respectively. These functional groups containing oxygen, nitrogen and sulphur are also confirmed using X-ray photoelectron spectroscopy (XPS). The XPS C 1s spectrum of FP-CNSs shows the C–O, C–N bonding and C(O)O bonding centred at 285.9 and 288.3 eV, respectively, with a main C–C bonding centred at 284.4 eV [Fig. 2(b)].

Two distinct peaks (531.3 and 532.7 eV) in the O 1s spectrum revealed the presence of oxygen atoms in the carbonyl groups and various other oxygen groups, as shown in Fig. 2(c). The chemical atmosphere of the nitrogen atoms was mostly in the form of pyridinic N and N-oxide centred at 398.6 and 402.8 eV, respectively [Fig. 2(d)]. The sulphur-bonding configuration in the S 2p spectrum is observed as the two bonding structures of C–S and C–SO_x centred at 164.2 and 169.0 eV, respectively [Fig. 2(e)]. The oxygen, nitrogen and sulphur contents were calculated as 20.5, 4.3 and 2.1 at% from the XPS results, respectively, and 24.1, 4.1, 3.8 wt% by elemental analysis (EA), respectively.

The lithium-ion storage behaviour of FM-CNSs was first investigated using a half-cell configuration in a voltage range from 1.5 to 4.5 V [Fig. 3(a)]. The cyclovoltammograms at a scan rate of 0.5 mV s^{-1} show a rectangular-like shape, with the additional redox couple at a potential range of around 3.2 V, which was not found in the cyclovoltammograms of oxygen-functionalised graphene nanosheets.[2] The additional redox reactions could originate from various functional groups on the surface of FM-CNSs such as nitrogen and sulphur groups. It has been demonstrated that nitrogen groups can work as redox centres.[17,18] Also, sulphur groups can contribute to Li ion storage as shown in Fig. S3.† At increasing scan rates, as

shown in Fig. 3(a), the additional redox peaks reduced, and a more rectangular-like shape was observed at a scan rate of 20 mV s^{-1}. This result suggests that charge storage in FM-CNSs was induced from both capacitive and faradic behaviours. The relatively slow kinetics of faradic reactions may lead to an increase in capacity in the low rate region, while the fast capacitive charge storage may contribute to the high rate performance. The galvanostatic charge/discharge profiles at scan rates from 0.2 to 20 A g^{-1} confirm the high capacity and rate performances of FM-CNSs [Fig. 3(c)]. FM-CNSs showed a specific capacity of 284 mA h g^{-1} at a scan rate of 0.2 A g^{-1}, and even at a rate 100-fold higher, 20 A g^{-1}, 64 mA h g^{-1} was achieved. These values reach a specific energy of 719 Wh kg^{-1} at a specific power of 1820 W kg^{-1}, and a specific power of 164 000 W kg^{-1} at a specific energy of 146 W kg^{-1} with a lithium metal anode. The energy and power densities of FM-CNSs surpass the previous results based on functionalised graphene; both the energy capacity (604 Wh kg^{-1} of H-GNSs) and power capacity (18 600 W kg^{-1} of M-GNSs) of oxygen-functionalised graphene.[2] To the best of our knowledge, this is one of the highest performance ever reported for nanoporous carbon electrodes. In addition, super-stable cyclic performances with a Coulombic efficiency of nearly 100% were achieved during 10 000 repetitive cycles at a current rate of 1 A g^{-1}. This superior cyclic stability is closely related to the properties of the solid–electrolyte-interface (SEI) layer on the surface of electrode materials. The SEI did not change significantly over many cycles possibly protecting the doped surface of carbon. In order to confirm the SEI layer on the surface of FM-CNSs, we performed *ex situ* XPS analysis after 10 charge/discharge cycles [Fig. S4†]. XPS C 1s and O 1s depth profiles of the FM-CNS electrode showed that the surface profile is different from the other depth profiles, indicating the presence of a SEI layer in which the C–O, C=O and Li–O bonds were mainly observed. The long-term cyclic stabilities could be achieved by the stable SEI layer that was formed in the initial charge/discharge process. In contrast, WCG-induced carbons with no activation agents showed a relatively poor electrochemical performance, although they had 21.5 at% oxygen functional groups as shown in Fig. S5.† This result suggests that a specific surface area and nanostructure are critical for electrochemical performance. Moreover, GNSs that had a specific surface area of 250 m^2 g^{-1} and 16.5 at% oxygen functional groups (Fig. S6†), exhibited a specific capacity of 150, 89 and 47 mA h g^{-1} at a current density of 0.2, 0.5 and 1 A g^{-1}, suggesting that doped nitrogen and sulphur in carbon structures also play an important role in lithium-ion storage.

This superior electrochemical performance of FM-CNSs is attributable to their unique characteristics as follows. Firstly, the numerous heteroatoms provide large active sites and enhanced electrical properties. Secondly, the highly porous microstructures and good wettability with electrolytes induced by the heteroatoms reduce blocked active sites so that all redox centres can fully participate in Li ion storage. Thirdly, nanostructures with a high aspect ratio (~9 nm thickness *vs.* several micrometres lateral size, >300), high electrical conductivity of
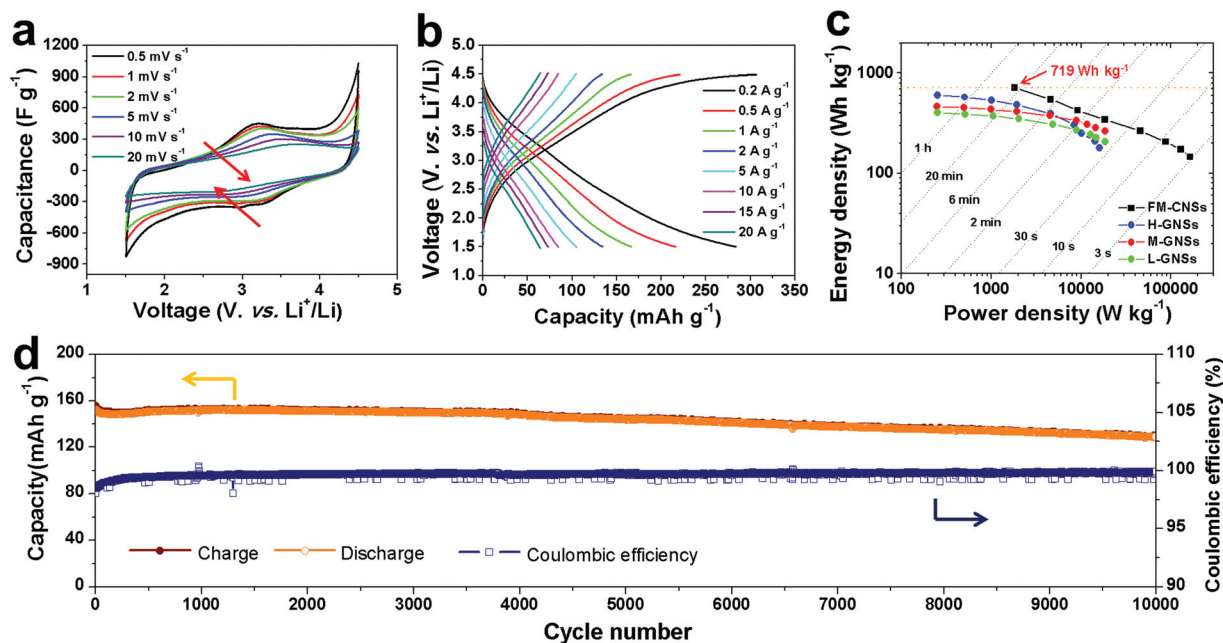
Fig. 3 Electrochemical performances of FM-CNSs in the potential range of 1.5–4.5 V. (a) Cyclovoltammograms at scan rates of 0.5, 1, 2, 5, 10 and 20 mV s^{-1}. (b) Galvanostatic charge/discharge profiles at current densities of 0.2, 0.5, 1, 2, 5, 10, 15 and 20 A g^{-1}. (c) Ragone plots of FM-CNSs (black square) and previous results based on graphene nanosheets, H-GNSs (blue circle), M-GNSs (red circle) and L-GNSs (green circle).[2] (d) Cyclic performance during 10 000 repetitive cycles at a current density of 1 A g^{-1}.

~120 S cm^{-1} and extensive surface area (~2100 m^2 g^{-1}), about eightfold larger than practical graphene-based electrodes (~250 m^2 g^{-1}), lead to superior rate performances, because surface-driven reaction kinetics can be limited by electron/ion transfer rates and active surface area. Fourthly, the microporous structure composed of numerous carbon nano-crystallites makes stress-free cycles, leading to stable cyclic performances.

The roles of heteroatoms in the pseudocapacitive lithium ion storage are investigated using first-principles calculations. The configuration of graphene nanoribbons terminated with hydrogen atoms on zigzag shaped edges is considered as reported.[31] After the model structures are fully relaxed, as shown in Fig. 4(a), heteroatoms such as oxygen, sulphur, nitrogen and their combinations are considered in the edge sites [Fig. S7†]. We found that heteroatoms in the edge sites of poly hexagonal carbon structures can be a redox centre for lithium ion storage by their synergistic effects. In the specific cases considered [Fig. 4(b)], neighbouring two oxygen atoms which bond to single lithium ion show the most stable thermodynamic structure (−3.11 eV). Fig. 4(c) illustrates additional charge populations between the lithium ion and the neighbouring two oxygen atoms, suggesting that there is a charge transfer. Also, in Bader charge analysis,[32] we can confirm that oxygen atoms (7.15, 7.14, respectively) obtained negative charges from lithium ions (0.1) (Table S1†). Possible structures and formation energies of various oxygen heteroatoms with lithium ions are exhibited in Fig. S8(a).† In contrast, sulphur
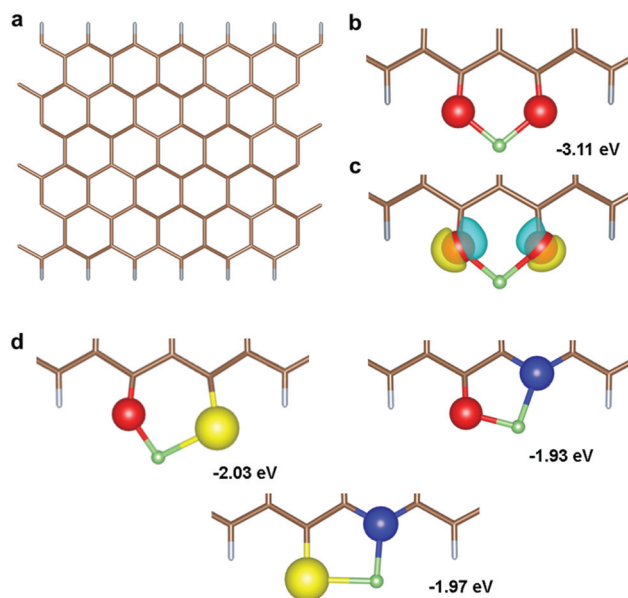

Fig. 4 (a) Top-viewed structure of graphene nanoribbon terminated with hydrogen atoms on zigzag shaped edges. (b) Configuration of neighbouring two oxygen atoms with lithium ion. (c) Isosurface of charge distribution in the neighbouring two oxygen atoms with lithium ion. Yellow and blue indicate the charge gained and lost, respectively. (d) Heteroatom combinations with lithium ion in the edge sites (brown, carbon; grey, hydrogen; red, oxygen; yellow, sulphur; blue, nitrogen; green, lithium).

heteroatoms in the edge sites show relatively unfavourable bonding characters with lithium ions, compared to the cases of oxygen groups [Fig. S8(b)†]. The same neighbouring two sulphur configuration with lithium ions also has unfeasible formation energy of 0.271 eV, while the neighbouring two oxygen heteroatoms with lithium ions show the most stable structure in all the oxygen structures. This could be due to stronger repulsive force between sulphur atoms, because the atomic radius (100 pm) of sulphur is much bigger than that (60 pm) of oxygen. The repulsive interaction makes the system unstable. For nitrogen heteroatoms, single lithium ion can be directly bonded to the nitrogen atom [Fig. S8(c)†]. However, the redox potential (0.73 V) is not suitable as a cathode for lithium ion storage. It is notable that different heteroatom combinations such as oxygen–sulphur, oxygen–nitrogen and sulphur–nitrogen show possibilities for redox reaction with lithium ions. For the oxygen–sulphur combination, the most feasible formation energy is −2.03 eV in the various possible configurations [Fig. 4(d)]. The oxygen–nitrogen and sulphur–nitrogen combinations also showed formation energy of −1.93 eV and −1.97 eV,

respectively [Fig. 4(d)], indicating that they can be redox centres for lithium ions. Although these calculation results are limited to a few possible combinations of dopants in model, they suggest that the electrochemical activity with lithium can be rationally tuned by the strategy of hetero-atomic doping in carbonaceous materials.

Full cell tests were carried out using the FM-CNSs as the cathode and various NCMs such as (i) sulphur-doped graphene nanosheets (S-GNSs), (ii) hierarchically porous carbon nano-fibres (HP-CNFs) and (iii) commercial graphite nanoplates (GNPs, XGNP-M-5, XG Science) as the anode. The material characteristics and lithium-ion storage behaviours of S-GNSs, HP-CNFs and GNPs are provided in Fig. S3 and ref. 8, and Fig. S9, and S10,† respectively. The asymmetric pseudo-capacitors were assembled using the samples pre-cycled by the half cell configuration. For example, the S-GNS electrode was pre-cycled with a lithium metal as a reference and counter electrode in potential range between 0.01 and 1.5 V. The FP-CNS electrode was also pre-cycled with lithium metal in the potential range between 1.5 and 4.5 V. Following the pre-cycles, the asymmetric pseudocapacitors were assembled
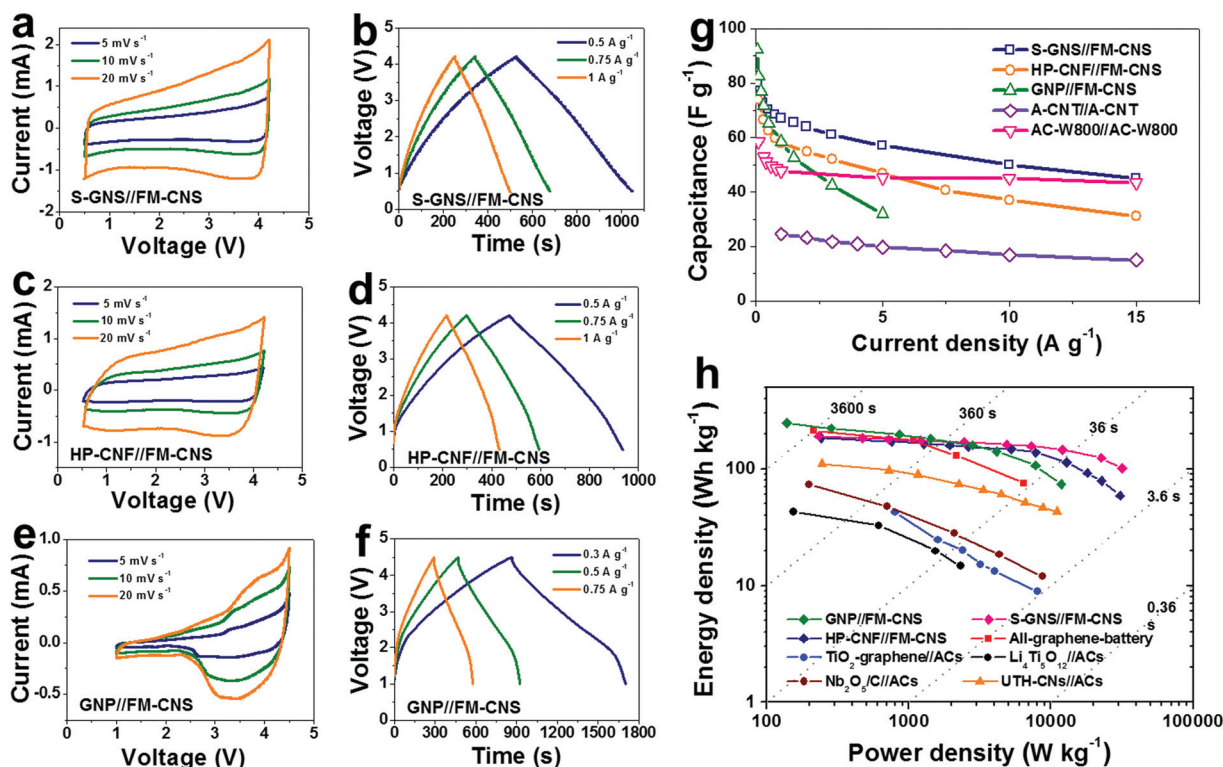

Fig. 5 Electrochemical analyses of the asymmetric lithium-ion pseudocapacitors based on S-GNS//FM-CNS and HP-CNF//FM-CNS in the range of 0.5–4.2 V, and GNP//FM-CNS in the potential range of 1–4.5 V. (a), (c), (e) Cyclovoltammograms at scan rates of 5 mV s^{-1} (navy), 10 mV s^{-1} (olive) and 20 mV s^{-1} (orange). (b), (d), (f) Galvanostatic charge/discharge profiles at 0.5 A g^{-1} (navy), 0.75 A g^{-1} (olive) and 1 A g^{-1} (orange) for S-GNS//FM-CNS and HP-CNF//FM-CNS, and at 0.3 A g^{-1} (navy), 0.5 A g^{-1} (olive) and 0.75 A g^{-1} (orange) for GNP-FM-CNS. (g) Rate performances of the S-GNS//FM-CNS (navy squares), HP-CNF//FM-CNS (orange circle) and GNP//FM-CNS (olive triangle) pseudocapacitors described here and electric double layer capacitors such as A-CNT//A-CNT (violet diamond)[16] and AC-W800//AC-W800 (pink inverted triangle)[36] as a function of the specific current. (h) Ragone plot of various lithium-ion pseudocapacitors, including S-GNS//FM-CNS (pink diamonds), HP-CNF//FM-CNS (navy diamonds) and GNP//FM-CNS (olive diamonds) described here, as well as devices based on UTH-CNs//ACs (orange triangles),[13] graphene//graphene (red squares),[15] Nb$_2$O$_5$/C//ACs (wine circles),[33] TiO$_2$-graphene//ACs (blue circles)[34] and LiTi$_5$O$_{12}$//ACs (black circles).[35]

using the S-GNS and FP-CNS electrodes as the anode and cathode, respectively (Fig. S11†). A similar method was applied for HP-CNFs//FM-CNSs and GNPs//FP-CNSs. The cyclovoltammograms and galvanostatic charge/discharge profiles of the asymmetric hybrid pseudocapacitors showed the reversible lithium-ion storage behaviours in large potential windows, from 0.5 to 4.2 V for S-GNS//FM-CNS [Fig. 5(a) and (b)] and HP-CNF//FM-CNS [Fig. 5(c) and (d)] and from 1 to 4.5 V for GNP//FM-CNS [Fig. 5(e) and (f)]. The cyclovoltammograms of S-GNS//FM-CNS and HP-CNF//FM-CNS pseudocapacitors exhibited a rectangular-like shape, indicating ideal capacitive charge storage behaviours with good power characteristics, while the cyclovoltammogram of GNP//FM-CNS pseudocapacitors shows a strong asymmetric redox peak in a relatively high potential range between 2.5 and 4.5 V, indicating that GNP//FM-CNS pseudocapacitors have higher energy characteristics. We performed the additional electrochemical characterization by varying the sweep rate of the CV in the range 0.1–100 mV s^{-1}, as shown in Fig. S12.† Assuming that the current obeys a power-law relationship as a function of voltage; $i = av^b$, during the sweep, where a and b are constants, the data of S-GNS//FM-CNS and HP-CNF//FM-CNS can be fitted using $b = {\sim}1$, suggesting that the electrochemical reaction is mostly surface-controlled. In contrast, the data of GNP//FM-CNS can be fitted using $b = {\sim}0.83$, the interplay between surface controlled and diffusion-controlled reactions. The average discharge voltage of GNP//FM-CNS pseudocapacitors was calculated as 2.85 V, which is higher than the 2.44 V and 2.62 V exhibited by S-GNS//FM-CNS and HP-CNF//FM-CNS pseudocapacitors, respectively. In addition, GNP//FM-CNS pseudocapacitors showed a higher capacitance of 92 F g^{-1} than the 80 F g^{-1} and 74 F g^{-1} exhibited by S-GNS//FM-CNS and HP-CNF//FM-CNS, respectively, at a current density of 0.1 A g^{-1} [Fig. 5(g)]. Thus, the GNP//FM-CNS pseudocapacitors display outstanding energy density of 248 W kg^{-1} at a power density of 139 W kg^{-1}, exceeding the previous results of the all-graphene-battery,[15] UTH-CNs//ACs,[13] Nb$_2$O$_5$/C//ACs,[33] TiO$_2$-graphene//ACs,[34] and LiTi$_6$O$_{12}$//ACs[35] [Fig. 5(h)].

Meanwhile, the rate capability of S-GNS//FM-CNS pseudocapacitors is worthy of note, which reaches 45 F g^{-1} at a high current density of 15 A g^{-1}. Up to a current density of 15 A g^{-1}, the S-GNS//FM-CNS pseudocapacitors maintained the higher specific capacitance in all the samples, and even, their capacitance values to 15 A g^{-1} are higher than those of symmetric electric double layer capacitors (EDLCs) based on activated carbons (AC-W800//AC-W800)[36] and activated carbon nanotubes (A-CNT//A-CNT).[16] The Ragone plot of S-GNS//FM-CNS pseudocapacitors shows a power density of 31 650 W kg^{-1} at an energy density of 100 Wh kg^{-1}, indicating the utmost value in the reported hybrid capacitors. Additionally, the volumetric energy and power densities of the pseudocapacitors are exhibited in Fig. S13.† The pseudocapacitors also showed good cyclic performances in repetitive charge/discharge cycles [Fig. S14†]. The HP-CNF//FM-CNS pseudocapacitors had capacitance retention of about 67% at a specific current of 300 mA g^{-1} after 2000 cycles.

Conclusions

We have described FM-CNSs as a new high power/energy electrode for pseudocapacitive energy storage devices. The FM-CNSs fabricated from the WCGs are composed of graphitic crystals with a nanometre-scale size and exhibited 2D-like nanosheet morphology (~9 nm thick) with microporous structure and a large specific surface area of 2100 m^2 g^{-1}. The anisotropic graphitic crystals functionalised by nitrogen and sulphur atoms provided a near metallic pathway for electron conduction, leading to high electrical conductivity of ~120 S cm^{-1}. In addition, the FM-CNSs inherently contained numerous redox active heteroatoms such as oxygen, nitrogen and sulphur which aided in efficient charge storage. In our first-principles calculations, it was found that the heteroatom combinations can be a redox centre for lithium ion storage. The FM-CNSs electrode exhibited remarkable pseudocapacitive lithium-ion storage behaviour as a cathode in asymmetric pseudocapacitors. The asymmetric system paired with various NCMs could deliver an unprecedentedly high energy density of 248 Wh kg^{-1} with a power density of 139 W kg^{-1} and great power density of 31 650 W kg^{-1} with an energy density of 100 W kg^{-1}, indicating the highest value in the reported hybrid capacitors. Stable cycle performance was demonstrated, with 67% of the initial capacitance following 2000 cycles at a specific current of 300 mA g^{-1}.

Experimental section

Preparation of the FM-CNSs

The WCGs, obtained from commercial beverage manufacturers, were treated ultrasonically using a horn-type sonicator in *N,N*-dimethylformamide (99.8%, Sigma-Aldrich, USA). The supernatant was vacuum-filtered and the solvent was exchanged using *t*-butanol. The exfoliated WCGs were frozen at −196 °C and then freeze-dried at −45 °C and 4.5 Pa for 72 h. The exfoliated WCGs (5 g) were mixed with 2.5 g KOH (95%, Samchun Pure Chemical Co., Ltd, Seoul, Korea) in a mortar and then heated to 800 °C for 2 h at a heating rate of 10 °C min^{-1}. The resulting products (FM-CNSs) were washed using distilled water and ethanol (99.9%, OCI Company, Atlanta, GA, USA) and then dried in a vacuum oven at 30 °C.

Characterisation

The morphology of the samples was observed using FE-TEM (JEM2100F, JEOL, Japan) and FE-SEM (S-4300, Hitachi, Japan). XRD (Rigaku DMAX 2500) analysis was performed using Cu-Kα radiation (with a wavelength λ = 0.154 nm) at 40 kV and 100 mA. Raman spectroscopy was carried out using a continuous-wave linearly polarised laser with a wavelength of 514 nm, a 50 μm diameter pinhole, and a 600 groove per mm grating. The porosity was analysed using nitrogen adsorption and desorption isotherms obtained from a surface area and a porosimetry analyser (ASAP 2020, Micromeritics, USA) at −196 °C. EA was carried out using an EA1112 (CE Instrument, Italy). XPS

(PHI 5700 ESCA) was performed using monochromated Al-Kα radiation ($h\nu$ = 1486.6 eV). FT-IR spectroscopy was carried out using a VERTEX 80v (Bruker Optics, Germany). To measure the electrical transport properties, an FM-CNS was deposited on 300 nm-thick SiO_2/highly p-doped Si wafers. The electrode was fabricated by electron beam lithography (acceleration voltage: 15 kV), followed by metal evaporation of Ti/Au (5/50 nm) under high vacuum (<1 × 10^{-3} Pa) and lift-off procedures. The temperature-dependent I–V characteristics were obtained using the two-probe method with a Janis cryogenic system and a semiconductor characterisation system (4200-SCS, Keithley) under vacuum (<0.2 Pa).

Electrochemical characterisation

The electrochemical properties of FM-CNSs, S-GNSs, HP-CNFs, GNPs and the asymmetric pseudocapacitors were characterised using a Wonatec automatic battery cycler and CR2032-type coin cells. For the half-cell tests, the coin cells were assembled with the samples as the working electrodes, and metallic lithium foil as both the reference and counter electrodes in a glove box filled with argon. LiPF$_6$ (1 M; Aldrich, purity: 99.99%) was dissolved in a solution of ethylene carbonate and dimethyl carbonate mixture (1 : 1 v/v), and was used as the electrolyte. A glass microfiber filter separator (GF/F, Whatman) was used as a separator. The working electrodes were prepared by mixing the active material (80 wt%) with conductive carbon (10 wt%) and polyvinylidene fluoride (10 wt%) in N-methyl-2-pyrrolidone. The resulting slurries were uniformly applied to the Cu for the S-GNSs, HP-CNSs, GNPs and Al foil for FP-CNSs. The electrodes were dried at 120 °C for 2 h and roll pressed. Mass loading of active materials was about 1 mg cm^{-2} for FM-CNSs, and the total electrode weight was about 2–3 mg. The asymmetric pseudocapacitors based on S-GNSs//FM-CNSs, HP-CNFs//FM-CNSs and GNPs//FP-CNSs were assembled using pre-cycled samples. The voltage was controlled to 1.5 V *versus* Li$^+$/Li. The pseudocapacitors were galvanostatically cycled between 0.5 V and 4.2 V for S-GNSs//FM-CNSs and HP-CNFs//FM-CNSs, and between 1 V and 4.5 V for GNPs//FM-CNSs at various currents. The specific capacitance of the pseudo-capacitors was determined from the galvanostatic measurements using

$$C = \frac{I_{\text{cons}}}{m\mathrm{d}V/\mathrm{d}t},$$

where I_{cons} is the (constant) current, m is the total mass of both carbon electrodes, and dV/dt was calculated from the slope of the discharge curve over the range from $V = V_{\max}$ (the voltage at the beginning of discharge) to $V = 1/2V_{\min}$. The specific energy and power were calculated from the galvano-static discharge profiles of the pseudocapacitors.

Computational details

All first-principles calculations were performed using the Perdew–Burke–Ernzerhof (PBE) exchange–correlation parametrization to density functional theory (DFT) with the spin-polarized generalized gradient approximation (GGA).[37] A plane-wave basis set and the projector-augmented wave (PAW) method were also used,[38,39] as implemented in the Vienna Ab-initio Simulation Package (VASP) code.[40] All calculations were performed based on a single nanoribbon layer, in which the edge sites are terminated with hydrogen atoms. A plane-wave basis set with a kinetic energy cutoff of 500 eV was used and appropriate numbers of k-points were used. All parameters in the calculation are considered to converge the total energy to 0.01 eV Å^{-1}. Quantification of charge transfer was performed with Bader charge analysis code. To describe a single nanoribbon layer, we constructed vacuum slab layered geometric models because of periodic boundary conditions in VASP. The thickness of the vacuum slabs were set to >15 Å in both y-direction and z-direction.[41]

Thermodynamic stability of lithium storage on oxygen, sulphur and nitrogen functional was calculated using defect formation energy (E_{f}) as follows:

$$E_{\mathrm{f}} = E_{\text{tot}} - E_{\text{substrate}} - n \times \mu_{\text{Li}}$$

where E_{tot} and $E_{\text{substrate}}$ are DFT total energies of the system with lithium and heteroatom and of nanoribbon layer with the heteroatom, respectively. n is the number of lithium ions attached to the heteroatom and μ_{Li} is chemical potential of lithium.

Notes and references

1 S. W. Lee, N. Yabuuchi, B. M. Gallant, S. Chen, B.-S. Kim, P. T. Hammond and Y. Shao-Horn, *Nat. Nanotechnol.*, 2010, **5**, 531.
2 H. Kim, H.-D. Lim, S.-W. Kim, J. Hong, D.-W. Seo, D.-C. Kim, S. Jeon, S. Park and K. Kang, *Sci. Rep.*, 2013, **3**, 1506.
3 H. Kim, Y.-U. Park, K.-Y. Park, H.-D. Lim, J. Hong and K. Kang, *Nano Energy*, 2014, **4**, 97.
4 W. Gu, N. Peters and G. Yushin, *Carbon*, 2013, **53**, 292.
5 G. Wang, X. Shen, J. Yao and J. Park, *Carbon*, 2009, **47**, 2049.
6 X. Li, D. Geng, Y. Zhang, X. Meng, R. Li and X. Sun, *Electrochem. Commun.*, 2011, **13**, 822.

7 L. Qui, W.-M. Chen, Z.-H. Wang, Q.-G. Shao, X. Li, L.-X. Yuan, X.-L. Hu, W.-X. Zhang and Y.-H. Huang, *Adv. Mater.*, 2012, **24**, 2047.

8 Y. S. Yun, V.-D. Le, H. Kim, S.-J. Chang, S. J. Baek, S. Park, B. H. Kim, Y.-H. Kim, K. Kang and H.-J. Jin, *J. Power Sources*, 2014, **262**, 79.

9 S. L. Candelaria, Y. Shao, W. Zhou, X. Li, J. Xiao, J.-G. Zhang, Y. Wang, J. Liu, J. Li and G. Cao, *Nano Energy*, 2012, **1**, 195.

10 J. Maier, *Nat. Mater.*, 2005, **4**, 805.

11 W. Lu and C. M. Lieber, *Nat. Mater.*, 2007, **6**, 841.

12 P. Simon, Y. Gogotsi and B. Dunn, *Science*, 2014, **343**, 1210.

13 Y. S. Yun, S. Y. Cho, H. Kim, H.-J. Jin and K. Kang, *ChemElectroChem*, 2015, **2**, 359.

14 B. Z. Jang, C. Liu, D. Neff, Z. Yu, M. C. Wang, W. Xiong and A. Zhamu, *Nano Lett.*, 2011, **11**, 3785.

15 H. Kim, K.-Y. Park, J. Hong and K. Kang, *Sci. Rep.*, 2014, **4**, 5278.

16 Y. S. Yun, G. Yoon, K. Kang and H.-J. Jin, *Carbon*, 2014, **80**, 246.

17 M. Lee, J. Hong, D.-H. Seo, D. H. Nam, K. T. Nam, K. Kang and C. B. Park, *Angew. Chem., Int. Ed.*, 2013, **52**, 8322.

18 J. Hong, M. Lee, B. Lee, D.-H. Seo, C. B. Park and K. Kang, *Nat. Commun.*, 2014, **5**, 5335.

19 J. Ding, H. Wang, Z. Li, K. Cui, D. Karpuzov, X. Tan, A. Kohandehghan and D. Mitlin, *Energy Environ. Sci.*, 2015, **10**, 1039.

20 R. W. Jenkins, N. E. Stageman, C. M. Fortune and C. J. Chuck, *Energy Fuels*, 2014, **28**, 1166.

21 F. Boudrahem, A. Soualah and F. Aissani-Benissad, *J. Chem. Eng. Data*, 2011, **56**, 1946.

22 A. Namanea, A. Mekarziab, K. Benrachedib, N. Belhaneche-Bensemraa and A. Hellal, *J. Hazard. Mater.*, 2005, **B119**, 189.

23 T. E. Rufford, D. Hulicova-Jurcakova, E. Fiset, Z. Zhu and G. Q. Lu, *Electrochem. Commun.*, 2009, **11**, 974.

24 T. E. Rufford, D. Hulicova-Jurcakova, Z. Zhu and G. Q. Lu, *Electrochem. Commun.*, 2008, **10**, 1594.

25 M. R. Jisha, Y. J. Hwang, J. S. Shin, K. S. Nahm, T. P. Kumar, K. Karthikeyan, N. Dhanikaivelu, D. Kalpana, N. G. Renganathan and A. M. Stephan, *Mater. Chem. Phys.*, 2009, **115**, 33.

26 W.-H. Chen and P.-C. Kuo, *Energy*, 2010, **35**, 2580.

27 V. V. Bhat, C. I. Contescu, N. C. Gallego and F. S. Baker, *Carbon*, 2010, **48**, 1331.

28 P. Sheng, *Phys. Rev. B: Condens. Matter*, 1980, **21**, 2180.

29 H. Xie and P. Sheng, *Phys. Rev. B: Condens. Matter*, 2009, **79**, 165419.

30 B. Xu, S. Hou, H. Duan, G. Cao, M. Chu and Y. Yang, *J. Power Sources*, 2013, **228**, 193.

31 K. A. Ritter and J. W. Lyding, *Nat. Mater.*, 2009, **8**, 235.

32 G. Henkelman, A. Arnaldsson and H. Jonsson, *Comput. Mater. Sci.*, 2006, **36**, 354.

33 E. Lim, H. Kim, C. Jo, J. Chun, K. Ku, S. Kim, H. I. Lee, I.-S. Nam, S. Yoon, K. Kang and J. Lee, *ACS Nano*, 2014, **8**, 8968.

34 H. Kim, M.-Y. Cho, M.-H. Kim, K.-Y. Park, H. Gwon, Y. Lee, K. C. Roh and K. Kang, *Adv. Energy Mater.*, 2013, **10**, 1002.

35 H. Kim, K.-Y. Park, M.-Y. Cho, M.-H. Kim, J. Hong, S.-K. Jung, K. C. Roh and K. Kang, *ChemElectroChem*, 2014, **1**, 125.

36 L. Wei, M. Sevilla, A. B. Fuertes, R. Mokaya and G. Yushin, *Adv. Energy Mater.*, 2011, **1**, 356.

37 J. P. Perdew, K. Burke and M. Ernzerhof, *Phys. Rev. Lett.*, 1996, **77**, 3865.

38 P. E. Blochl, *Phys. Rev. B: Condens. Matter*, 1994, **50**, 17953.

39 G. Kresse and D. Joubert, *Phys. Rev. B: Condens. Matter*, 1999, **59**, 1758.

40 G. Kresse and J. Furthmuller, *J. Comput. Mater. Sci.*, 1996, **6**, 15.

41 Y.-W. Son, M. L. Cohen and S. G. Louie, *Phys. Rev. Lett.*, 2006, **97**, 216803.